crystals

MDPI

Article

The Epitaxial Growth of Ge and GeSn Semiconductor Thin Films on C-Plane Sapphire

Emmanuel Wangila [1,2,*], Calbi Gunder [1,2], Petro M. Lytvyn [3], Mohammad Zamani-Alavijeh [4], Fernando Maia de Oliveira [1], Serhii Kryvyi [1], Hryhorii Stanchu [1], Aida Sheibani [4], Yuriy I. Mazur [1], Shui-Qing Yu [5] and Gregory Salamo [1,2,4]

1 Institute for Nanoscience and Engineering, University of Arkansas, Fayetteville, AR 72701, USA; cjgunder@uark.edu (C.G.); fmaiade@uark.edu (F.M.d.O.); skryvyi@uark.edu (S.K.); hstanchu@uark.edu (H.S.); ymazur@uark.edu (Y.I.M.); salamo@uark.edu (G.S.)
2 Materials Science and Engineering, University of Arkansas, Fayetteville, AR 72701, USA
3 VE Lashkaryov Institute of Semiconductors Physics, NAS of Ukraine, 03028 Kyiv, Ukraine; plyt@isp.kiev.ua
4 Department of Physics, University of Arkansas, Fayetteville, AR 72701, USA; mzamania@uark.edu (M.Z.-A.); asheiban@uark.edu (A.S.)
5 Department of Electrical Engineering, University of Arkansas, Fayetteville, AR 72701, USA; syu@uark.edu
* Correspondence: eswangil@uark.edu

Abstract: $Ge_{1-x}Sn_x$ growth on a new sapphire platform has been demonstrated. This involved the growth of GeSn on Ge/GaAs layers using the algorithm developed. The resultant growths of Ge on GaAs/AlAs/sapphire and $Ge_{1-x}Sn_x$ on Ge/GaAs/AlAs/sapphire were investigated by in situ and ex situ characterization techniques to ascertain the surface morphology, crystal structure, and quality. The growth mode of Ge on GaAs was predominantly two-dimensional (2D), which signifies a layer-by-layer deposition, contributing to enhanced crystal quality in the Ge/GaAs system. The growth of $Ge_{1-x}Sn_x$ with 10% Sn on a graded profile for 30 min shows uniform composition and a strong peak on the reciprocal space map (RSM). On the other hand, the partially relaxed growth of the alloy on RSM was established.

Keywords: partially relaxed GeSn; surface relief; vibrational modes; grading profile

check for updates

Citation: Wangila, E.; Gunder, C.; Lytvyn, P.M.; Zamani-Alavijeh, M.; Maia de Oliveira, F.; Kryvyi, S.; Stanchu, H.; Sheibani, A.; Mazur, Y.I.; Yu, S.-Q.; et al. The Epitaxial Growth of Ge and GeSn Semiconductor Thin Films on C-Plane Sapphire. *Crystals* **2024**, *14*, 414. https://doi.org/10.3390/cryst14050414

Academic Editor: Serguei Petrovich Palto

Received: 12 April 2024
Revised: 23 April 2024
Accepted: 25 April 2024
Published: 28 April 2024

Copyright: © 2024 by the authors. Licensee MDPI, Basel, Switzerland. This article is an open access article distributed under the terms and conditions of the Creative Commons Attribution (CC BY) license (https://creativecommons.org/licenses/by/4.0/).

1. Introduction

GeSn semiconductor thin films grown on Ge or Si substrates have shown significant potential for near-infrared and mid-infrared [1] lasers, detectors, waveguides, modulators, and electronics, such as field effect transistors, all on a single platform [2,3]. Success could advance research efforts in microwave photonics [4]. To realize this potential, the challenge today is to achieve the growth of high-quality GeSn with low misfit and threading dislocations while maintaining Sn content at the order of 20% or more [5]. The roadblock to this goal is that on one side, a high Sn content is needed to transition the indirect band gap of Ge to a direct band gap and to tune the band gap to mid-infrared wavelengths. On the other side, high Sn content leads to a notable lattice mismatch of 14.7% with Ge [3,6–9] and 17% with Si substrates, resulting in the introduction of substantial misfit and threading dislocations. In addition, the low solubility of Sn in Ge (~1%) [10–15] has resulted in Sn segregation from high Sn samples [16,17]. Consequently, significant defect density and Sn segregation impact the electrical and optical properties of GeSn and discourage and limit applications [10,18]. As a result, there is much merit to the pursuit of growth techniques with the potential to produce GeSn thin films with about 20% Sn and low misfit and threading dislocations without Sn segregation.

In this paper, we report on an investigation of a growth technique using an ultra-high vacuum (UHV) molecular beam epitaxy (MBE) chamber for the fabrication of high-quality, high Sn content, Ge and GeSn thin films on a sapphire/III-V semiconductor substrate. The

choice of a sapphire platform is based on (1) a high index contrast for efficient waveguides, (2) the advantages of sapphire for microwave electronics, and (3) our research on high-quality III-V semiconductors grown on sapphire [19], all potentially allowing higher function at a reduced cost. The technique we investigated to grow GeSn on sapphire uses both a composition gradient and growth temperature gradient to produce a corresponding linear Sn composition that achieves GeSn on a sapphire substrate with a greater than 10% Sn content. To examine and demonstrate the quality of the GeSn, we employed multiple characterization techniques, including (i) in situ reflection high-energy electron diffraction (RHEED), as well as ex situ (ii) high-resolution X-ray diffraction (HR-XRD), (iii) Raman spectroscopy, and (iv) photoluminescence (PL). The knowledge obtained by these characterization tools was then used to compare thin film growths with and without the use of a gradient transition layer. The outcome was that by using these characterization techniques, we demonstrated the high-quality growth of GeSn thin films with the potential to reach 20% Sn content. Importantly, since sapphire is already an ideal substrate for microwave electronics [20–23], with the integration of GeSn at 10 to 20% Sn, we have the exciting opportunity to explore microwave photonics on a single sapphire chip.

2. Materials and Methods

In this research, GeSn films were fabricated on a prepared sapphire wafer using molecular beam epitaxy (MBE) interconnected UHV chambers. Knudsen cells supplied Al, Ge, and Sn, while an As reservoir equipped with a cracker provided As. For this investigation, hydrofluoric acid was used to etch the sapphire wafer surface to create a terraced surface, followed by rinsing with deionized water and baking in a degas chamber before growth. With this treatment, we achieved a surface roughness of 2.2 Å or less as our starting sapphire wafer. This was followed by the growth of a 5 nm thick AlAs layer on the sapphire wafer at 700 °C prior to the deposition of a thicker GaAs layer and Ge layer. The sapphire/AlAs/GaAs/Ge substrate preparation is based on a recipe, as described in our previous work [4], and acts as the substrate for the growth of GeSn. In Section 3.1, we describe three sapphire/AlAs/GaAs/Ge substrates that were prepared as shown in Figure 1a–c. In Section 3.2, GeSn layers were epitaxially grown on the prepared substrates (Figure 1d) using a special algorithm applied to the Sn cell to produce a linear Sn flux gradient [24]. The precise thickness control was attained by calibrating growth rates for AlAs, GaAs, and GeSn and ensuring consistent film thickness during growth. After growth, ellipsometry was used to confirm the thickness of the layers.

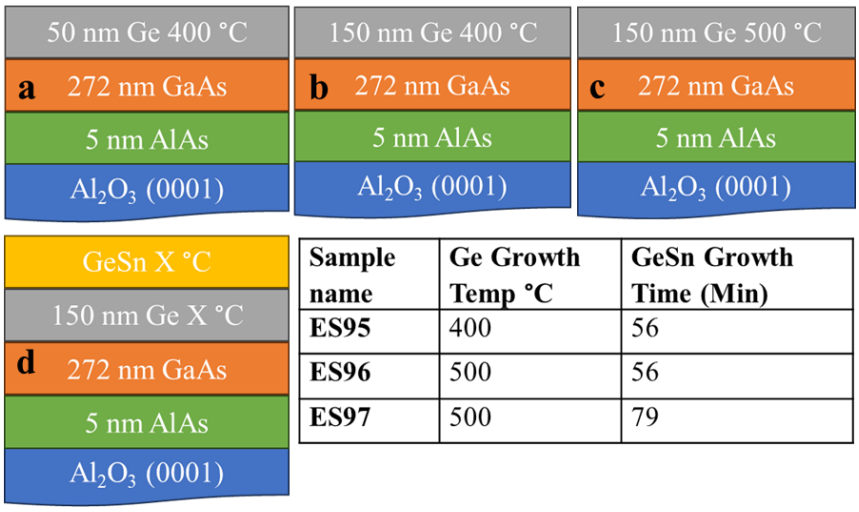

Sample name	Ge Growth Temp °C	GeSn Growth Time (Min)
ES95	400	56
ES96	500	56
ES97	500	79

Figure 1. Schematic of (**a**) 50 nm of Ge grown at 400 °C, (**b**) 150 nm of Ge grown at 400 °C, (**c**) 150 nm of Ge grown at 500 °C, and (**d**) GeSn grown on a Ge layer fabricated at different temperatures listed in the inset table.

In addition to a gradient in the Sn flux, we simultaneously used a gradient to offset the change in growth temperature due to the changing flux from the growth cells [25]. We started the growth with the manipulator temperature at 200 °C and set the ramp rate at 10 °C/min, with the final achievable temperatures stopping near 74 °C at the end of the growth. Together, the Sn flux gradient and growth temperature gradient were used to achieve a linearly increasing composition of Sn and corresponding compressive strain. While the strain gradient drives Sn dominantly out of the surface, both the Sn gradient and temperature gradient drive Sn into the material, enhancing the Sn content during growth. The inset table in Figure 1 describes the conditions during GeSn growth.

After the growth of Ge or GeSn, the samples were immediately characterized to assess quality using the following: (1) Bruker's NanoScope III Dimension 3000TM atomic force microscope (AFM) manufactured in USA (Billerica, MA) to examine the surface morphology; (2) a Philips X'pert HR-XRD system from Netherlands (Almelo) that includes a four-bounce Ge (220) monochromator, a 1.8 kW $Cu_{K\alpha 1}$ X-ray tube and a Pixel X-ray detector to investigate crystallinity and strain; and (3) a 632.8 nm He-Ne laser, Olympus BX41 microscope manufactured in Japan (Hatagaya)., thermoelectrically cooled Si charge-coupled detector (CCD), and Horiba Jobin-Yvon LabRam HR spectrometer manufactured in France (Lille) to capture the Raman spectrum for the Sn content and strain. Finally, the photoluminescence (PL) measurements were performed at the temperature of 10 K using the standard off-axis setup configuration with the lock-in technique. A 1064 nm laser was used, and the emissions were collected using a Horiba iHR 550 grating-based spectrometer manufactured in France (Lille) equipped with a PbS detector.

3. Results

3.1. The Growth of Ge Using GaAs Buffer on C-plane Al_2O_3

For growth, the GaAs layers were epitaxially grown in a group III-V semiconductor materials UHV chamber and then transferred under a vacuum to an interconnected UHV chamber for the growth of group IV semiconductor materials. Three different samples were fabricated in this way (Figure 1a–c) and are discussed here. For all three samples, two-step growth of the GaAs layer to 272 nm thick was observed. The low-temperature GaAs were grown at 600 °C and the high-temperature GaAs were grown at 700 °C, with annealing at 800 °C [4]. This was followed for the two samples in Figure 1a,b with growth at 400 °C for the layer of Ge with thicknesses of 50 nm and 150 nm and one sample in Figure 1c with 150 nm of Ge grown at 500 °C. For each sample, AFM was used to determine the surface morphology and roughness of the Ge epilayer. Figure 2 shows the AFM images for the three samples. There appear to be directional-dependent features on the material topography. This anisotropy in surface features is more visible in Figure 2a,b as opposed to Figure 2c. A 50 nm Ge film grown at 400 °C initially exhibits relief growth patterns similar to the (111) GaAs layer beneath it, as Ge tries to mimic the underneath layer. The 150 nm Ge film grown at 400 °C and 500 °C, on the other hand, hides the features of the GaAs layer beneath. At 500 °C in Figure 2c, the temperature might have contributed to the coalescing of the Ge layer while leaving regions with vacancies in the form of pores (nearly round holes). Triangular growing inverted pyramids are clearly seen in Figure 2a,b. The facets of these pyramids and other crystallography-determined features form a pronounced anisotropy in the angular slope histograms (inset in Figure 2). The inclination of the facets of growth pyramids mainly varies from 9 to 30 degrees and can reach up to 50 degrees on the surface, as shown in Figure 2d. These facets correspond to the following set of crystallographic planes {577}, {122}, {112}, {133}, {113} and even planes {115} and {100} for the surface Figure 2c.

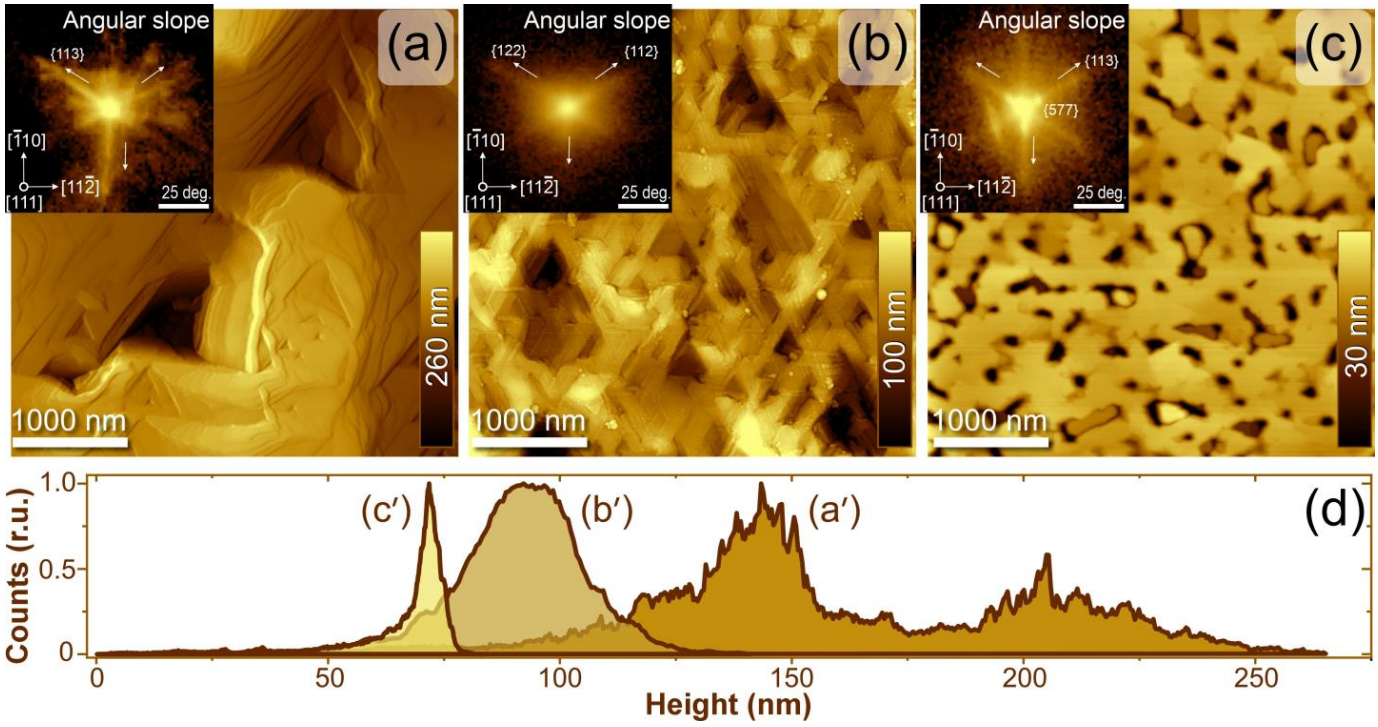

Figure 2. AFM images of Ge top layers on Al_2O_3/AlAs/GaAs structure: (**a**) the 50 nm thick Ge film grown at 400 °C (sample ES85); (**b**) 150 nm thick film grown at 400 °C (sample ES89) and (**c**) 150 nm thick film grown at 500 °C (sample ES103). Corresponding relief height histograms are shown in (**d**) as a′, b′ and c′. Insets illustrate the bivariate surface slope histograms. Cartesian coordinates are used.

A study of the crystal structure of Ge layers after growth was conducted by X-ray diffraction (XRD). The symmetric scan of $\omega/2\theta$ was taken with $\omega = 2\theta$, and the scanned planes are parallel to the sample surface. The presence of Ge (111) and Al_2O_3 (0006) diffraction peaks in Figure 3 indicates that the (111) growth of Ge on Al_2O_3 (0001) occurred. The Ge (111) peaks near the bulk Ge peak (vertical dashed line) indicate only a small level of strain in the Ge layer of all samples. The Phi scan was conducted to determine the azimuthal orientation relationship between Ge (111) and the Al_2O_3 (0001) substrate, utilizing Ge (220) and Al_2O_3 $(10\bar{1}2)$ reflections, respectively. A single crystal of Ge (111) exhibits three peaks separated by 120° due to its threefold symmetry. This plot has six peaks with 60° in-plane separation, indicating twin domains. The peaks with the highest intensity are separated by 120°, signifying one twin domain (or orientation), while the peaks with low intensity are in the other twin domain. This suggests that one orientation has higher formation energy than the other, which leads to the possibility of having a greater area under these peaks. The ratio of the summation of the areas of the highest intensity peaks to the lowest intensity is highlighted in Table 1 below.

Additionally, the linewidth of the XRD ω scan Ge(111) plane was compared to investigate the structural quality of the Ge epilayers. Linewidth is influenced by lateral correlation length and dislocation density [26,27]. The linewidth results, obtained through Gaussian fitting with an error bar of 0.001, demonstrate a substantial improvement compared to our prior findings on germanium (Ge) growth using AlAs nucleation [19,28]. Specifically, sample ES85 showcased a notably narrower linewidth that indicated enhanced crystal quality. In contrast, samples ES89 and ES103 exhibited nearly identical linewidths but not far from that of ES85. The detailed full width at half maximum (FWHM) values are presented in Table 1 below, providing a comprehensive comparison of the outcomes.

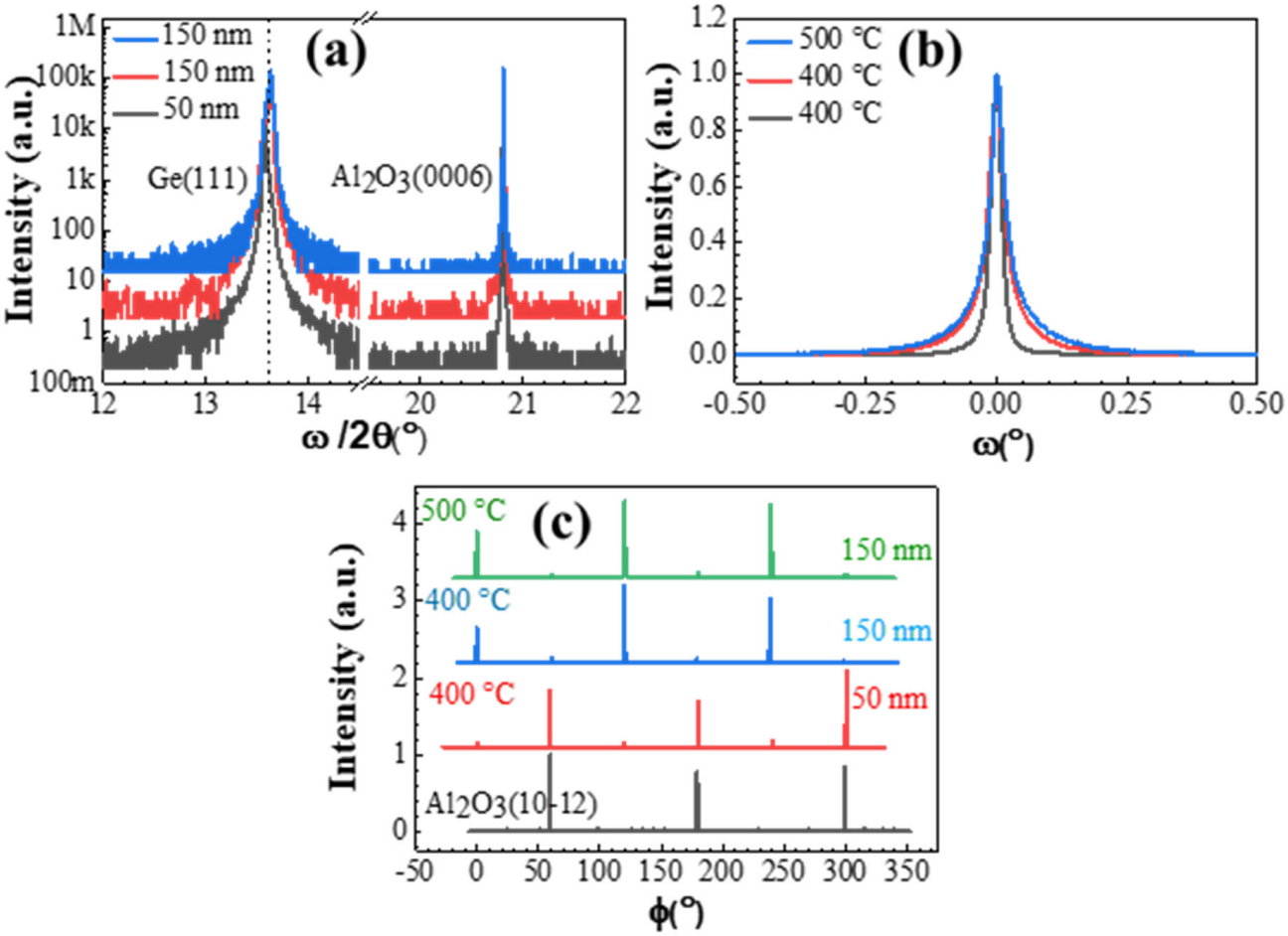

Figure 3. (**a**) Omega-2Theta scan of the sample, (**b**) Omega scan, and (**c**) Phi scan.

Table 1. Summary of the Ge growth temperature, full width at half maximum surface roughness, twinning ratios, and Raman shift.

Parameter	Sample Name		
	ES 85	**ES 89**	**ES 103**
Growth temp (°C)	400	400	500
Ge thickness (nm)	50	150	150
FWHM (deg)	0.024 ± 0.001	0.033 ± 0.001	0.03435 ± 0.001
Surface roughness (nm)	29.1	14.0	5.78
Twinning ratio %	8.85	5.0	8.45
Raman shift (cm^{-1})	−1.4	−0.4	−2.99

The initiation of germanium (Ge) growth on GaAs was marked by streaky RHEED images see Figure 4, and this characteristic was maintained throughout the growth period. The narrow linewidth in X-ray diffraction corresponds to these consistently streaky RHEED patterns, indicative of improved crystalline quality in the growing Ge material.

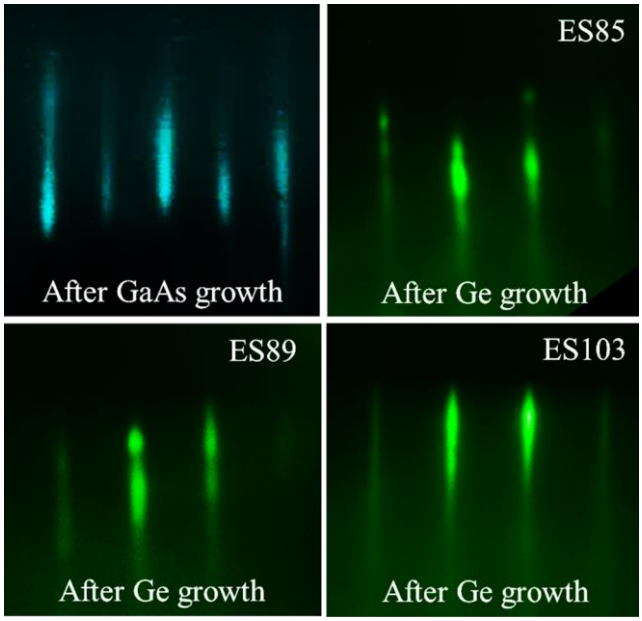

Figure 4. The RHEED images of GaAs and Ge after growth in III-V and IV chambers, respectively.

Since the lattice constants of Ge and GaAs are almost identical, the XRD Omega-2 theta reveals their diffraction peak at nearly the same place, superimposed on each other. Since GaAs and Ge each display a different vibrational spectrum, with the transverse optical Raman mode of GaAs reported at 267 cm^{-1} [29], and the triply degenerated optical Raman mode of the Ge mode at 300 cm^{-1} [30], Raman spectroscopy was utilized to confirm the epitaxy of Ge on the GaAs layer. The He-Ne laser of the 632.8 nm wavelength used as a Raman probe limited the optical penetration depth into the sample to only about 80 nm. An optical microscope with 1 μm spatial resolution was used to probe the Raman spectrum across three different areas on the samples. With samples grown at 400 °C, the 50 nm (ES85) exhibited large areas with pores or vacancies compared to 150 nm (ES89), as seen on the AFM images in Figure 2 and the micro-Raman shown in Figure 5. Areas with pores or vacancies exhibited a higher intensity of the GaAs mode than areas covered with Ge film. ES89 experienced a lower Raman shift than ES85, indicating that the film relaxes as the thickness increases, likely due to strain relaxation. Concerning the Ge film grown at 500 °C, the GaAs mode intensity is barely discernible. This indicates Ge epitaxy on the anisotropic surface of the GaAs layer, with vacancies filled by Ge. This is evidenced by the low GaAs mode intensity. The predominance of the Ge mode is observed as the He-Ne laser penetrates through the approximately 80 nm thick Ge film. Reduced vacancies can be attributed to Ge coalescing, resulting in diminished pores. However, this sample displayed a significant Raman shift compared to that grown at 400 °C, possibly due to increased strain or differences in defect density. These results confirm epitaxial Ge growth on GaAs, as shown in Figure 5, while Raman shift values are tabulated in Table 1.

Figure 6 presents the photoluminescence (PL) spectra acquired from the three Ge-grown samples and Ge reference samples captured at a temperature of 10 K. In examining the three samples, the influence of growth conditions on their optical properties became apparent. The first sample, grown at 400 °C with a thickness of 50 nm, did not exhibit any emission. In contrast, the third sample, grown at 500 °C with a thickness of 150 nm, displayed emissions; however, this occurred with a lower intensity compared to the sample grown at 400 °C with an expected thickness of 150 nm. The unique behavior of the latter sample, showing low-temperature PL with reduced intensity, suggests that the growth conditions played a role in altering its optical characteristics. Notably, samples with PL exhibited a red shift in the wavelength compared to the reference sample, indicating changes in the transitions to lower energy. The lower intensity observed in the 500 °C

grown sample is attributed to the coalescing of Ge adatoms and desorption during the growth process. This phenomenon leads to the formation of a thinner layer of Ge, sharing similarities with the 50 nm sample that did not exhibit emissions. The observed differences in emission intensity among these samples highlight the significance of growth conditions, specifically temperature, in influencing the coalescence and desorption processes, which ultimately affect the optical properties of the material.

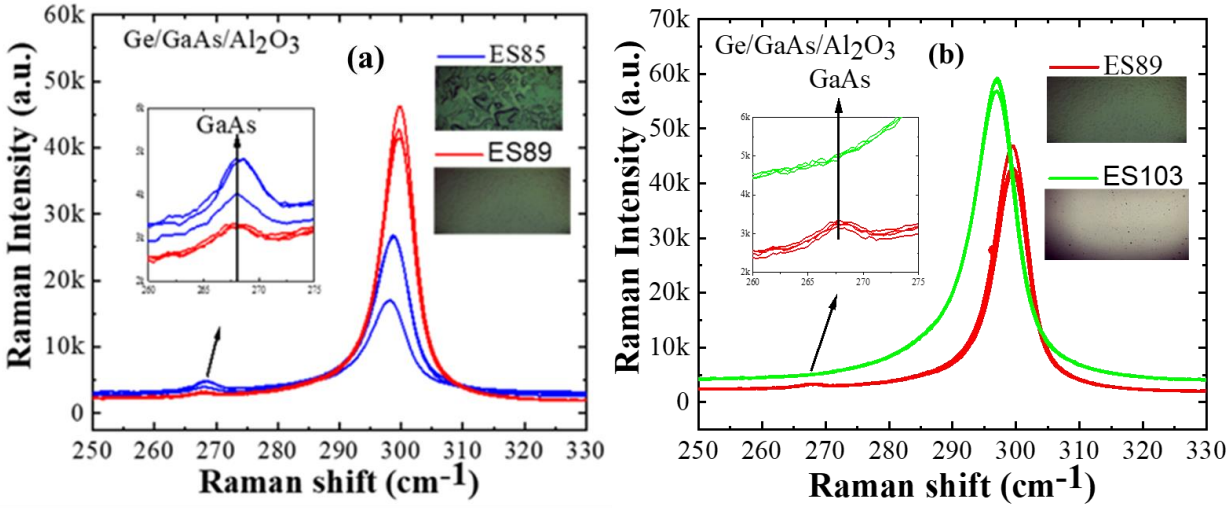

Figure 5. Raman spectra of (**a**) ES85 and ES89 (both grown at 400 °C) and (**b**) ES89 and ES103 (both having 150 nm Ge). The GaAs and Ge modes were acquired at 3 different spots of each sample. The micrographs, about 80 μm wide horizontally, show the surface of these samples.

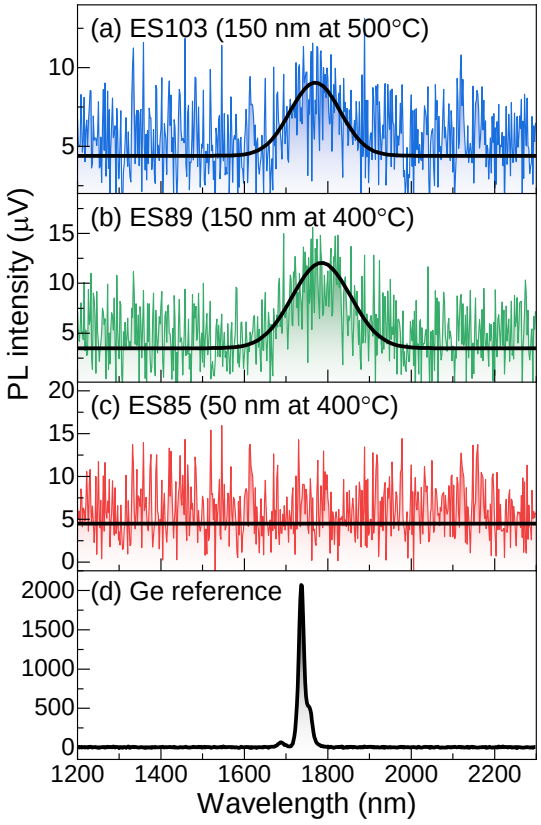

Figure 6. Low-temperature PL for (**a**) ES103 (150 nm Ge) grown at 500 °C, (**b**) ES85 (150 nm Ge) grown at 400 °C, (**c**) ES85 (50 nm Ge) grown at 400 °C, and (**d**) Ge reference sample.

3.2. Growth of GeSn on Ge buffer

Based on our results for Ge on the GaAs described above, we investigated the growth of GeSn on both the 150 nm of Ge grown at 400 °C and at 500 °C on the GaAs/sapphire-prepared substrate. The growth employed an algorithm developed to produce a linear Sn gradient in the growth of the GeSn. This was accomplished by varying and controlling both the Sn cell temperature gradient and the substrate temperature gradient. This also overcame the problem of substrate heating due to the optical flux from the growth cells when they were suddenly opened. The sample ES95 was grown on a 400 °C Ge buffer, while the other two samples, ES96 and ES97, were grown on a 500 °C Ge layer. All samples were characterized by AFM, XRD, PL, and micro-Raman tools to analyze surface morphology, crystallinity, strain, and GeSn composition. Additionally, secondary ion mass spectrometry (SIMS) characterization was employed to validate gradient alloying. The AFM shows the surface morphology of GeSn samples as shown in Figure 7. On GeSn films grown on Ge fabricated at 500 °C, it is noteworthy that the vacancies observed on the Ge/GaAs layer in Figure 2 persist, although to a lesser extent for GeSn grown on Ge at 400 °C. This persistence suggests that the underlying Ge layer itself exhibits some anisotropy in surface features. This anisotropy may be transferred to the GeSn epilayer during growth. Within this temperature range, conducive to the controlled incorporation of Sn atoms into the Ge crystal lattice without significant desorption issues, the reduction in visible vacancies implies improved epitaxial growth conditions. Nevertheless, the presence of vacancies in the GeSn epilayer can still be ascribed to various factors. These factors include lattice mismatch, anisotropy, defects, and disparities in crystal structures between GeSn and the underlying GaAs/Ge layer. The height scale bars have the same spacing of 40 nanometers to observe the surfaces' fine structure. The magnified view of fine-grain structures is shown in the inset. The starting height indicates the maximum depth of desorbed surface features. Average grain size and standard deviations are as follows: 35 ± 7 nm, 63 ± 17 nm, and 88 ± 22 nm for samples ES95, ES96, and ES97, respectively. The grain size for ES96 and ES97 differs due to a growth time of 27 min. Table 2 summarizes the growth time and surface roughness of the samples.

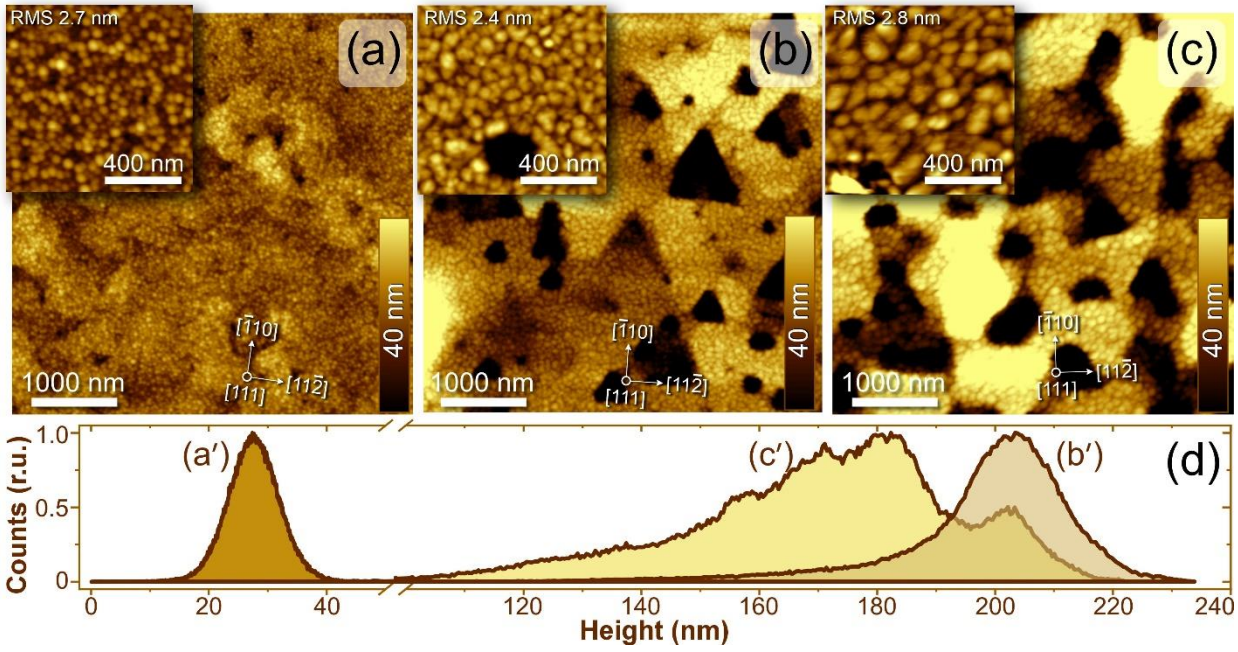

Figure 7. AFM images of GeSn top layers on the Al_2O_3/AlAs/GaAs/Ge structure: (**a**) the 200 nm thick GeSn film grown at 400 °C (ES95), (**b**) the 200 nm thick films grown at 500 °C (ES96), and (**c**) the 280 nm thick films grown at 500 °C (ES97). Corresponding relief height histograms are shown in (**d**) as a′, b′ and c′. Insets show the fine structure of grains.

Table 2. Summary of growth temperature, growth time and surface roughness of the three samples.

Parameter	Sample Name		
	ES95	**ES96**	**ES97**
Growth temperature of Ge layer (°C)	400	500	500
Surface roughness (nm)	3.56	11.5	16.2
Surface roughness in inset image (nm)	2.8	2.4	2.7
GeSn growth time (min)	56	56	79
GeSn thickness (nm)	~300	~300	~429

To establish whether we have a GeSn film on the epilayer, Raman spectra were taken see Figure 8. The micrograph clearly shows distinct areas on the GeSn film surface. Sample ES95 shows distinct smooth and rough areas, while ES97 shows a surface with uniform roughness that matches AFM data. The Raman spectra were taken at five different spots covering these two regions. All the samples displayed a GeSn Raman mode at around 252 cm^{-1} [31]. The Ge layer seems to have been strained when GeSn was grown on it. A shift to a lower wavenumber of Ge bulk from 300 cm^{-1} suggests that the vibrational modes associated with Ge-Ge bonds change as Sn is incorporated into the matrix of Ge due to the in-plane strain [32,33]. The decreasing intensity of the Ge-Ge Raman modes reflects the weakened vibrational modes caused by Sn incorporation, which disrupts the Ge-Ge regular bonding pattern. This agrees with Oehme et al.'s [34] observation that Ge-Ge intensity decreases with an increase in Sn incorporation.

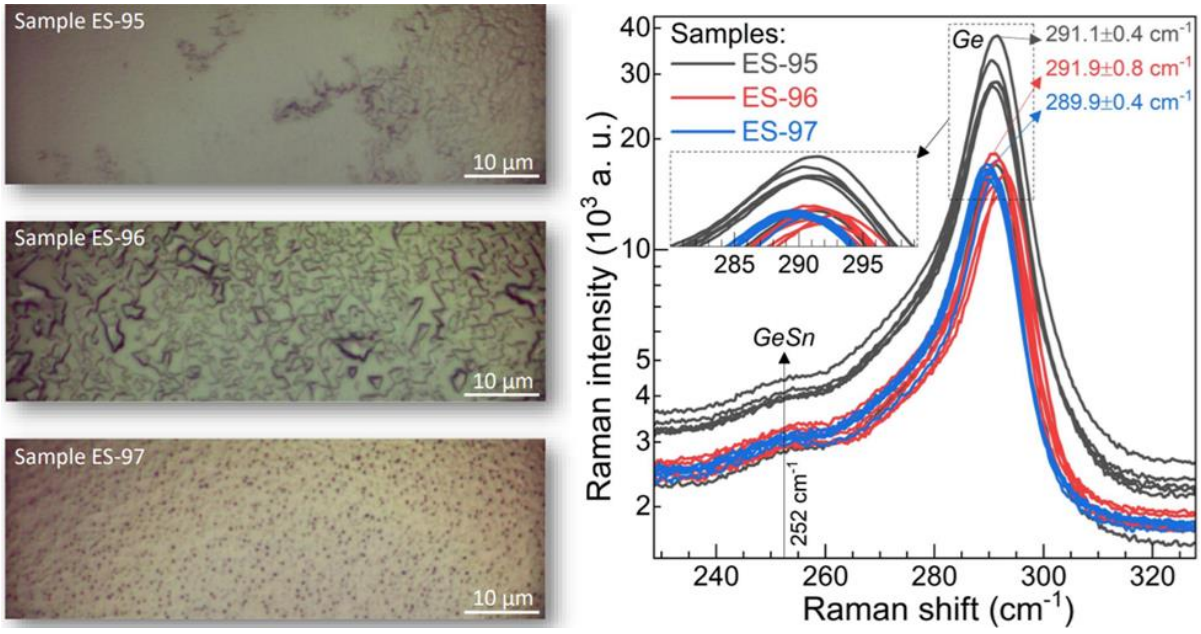

Figure 8. On the left, micrographs showing the clear and cloudy areas with distinct roughness. On the right are the Raman spectra taken at the clear and cloudy regions of GeSn films.

The XRD measurements were performed to determine the Sn content and strain in the GeSn layers of samples ES95, ES96, and ES97. In Figure 9a, the surface-symmetrical $2\theta/\omega$ scans show Ge(333) and GaAs(333), which overlap, and GeSn(333) diffraction peaks along with Al_2O_3(00012), which confirms the [111] growth of Ge and GeSn on the Al_2O_3(0001) substrate. For samples ES95 and ES97, the Ge peak slightly deviates from the Ge reference (vertical dashed line), indicating the presence of residual strain (Table 3) in the Ge buffer. The compositionally graded GeSn layer is seen on the $2\theta/\omega$ profiles as an elongated tail towards the lower diffraction angles. In Figure 9b–d, the XRD RSMs of Ge(135) reflection

reveal the partially relaxed growth of the GeSn layers. As can be seen, the degree of strain relaxation increases with the increasing Sn content. For sample ES97, the formation of a uniform composition of the GeSn layer with 10% Sn is concluded from the emergence of a strong GeSn peak on the RSM. The emergency of this strong peak is a result of 30 min of GeSn growth after ending Sn's grading profile. This differs from ES96, with a weak peak with only 7 min of GeSn growth after terminating the grading profile. For each sample, the maximal Sn fraction and the corresponding strain are listed in Table 3. The Sn content and the magnitude of strain were estimated by solving the expression for the biaxial strain as follows [35]:

$$\varepsilon_{\perp} = -\frac{2C_{11} + 4C_{12} - 4C_{44}}{C_{11} + 2C_{12} + 4C_{44}}\varepsilon_{\parallel}$$

where $\varepsilon_{\perp} = \left(d_{\perp}^{exp} - d_{\perp}^{ref}\right)/d_{\perp}^{ref}$ and $\varepsilon_{\parallel} = \left(d_{\parallel}^{exp} - d_{\parallel}^{ref}\right)/d_{\parallel}^{ref}$ are the vertical and lateral strains, and C_{11}, C_{12}, and C_{44} are the elastic constants.

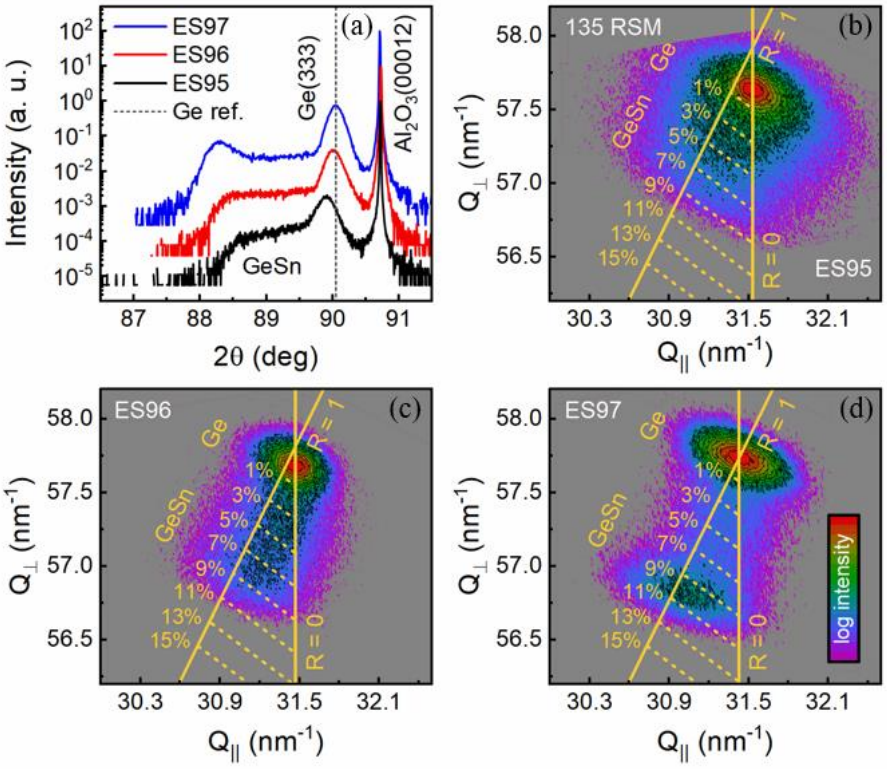

Figure 9. XRD and RSM for samples ES95, ES96, and ES97. (**a**) The 2 theta−Omega scans showing GeSn, Ge, and Al_2O_3 peaks; (**b**–**d**) the RSM of GeSn/Ge as measured from 135 crystal plane.

The crystal quality assessment utilized Omega rocking curves in the high-resolution configuration, conducted at four distinct locations spanning the entire Omega-2theta range of the gradient GeSn(111) peak, as illustrated in Figure 10. The observed trend of FWHM during the growth of Ge and graded GeSn alloys unveiled a significant evolution in crystal quality. It should be noted that the Ge(111) peak overlapped with the GaAs(111) buffer layer. Therefore, the Omega scan of this peak was fitted with broad and narrow Gaussian peaks, indicating varying degrees of crystalline perfection. However, it is still difficult to distinguish which peak corresponds to which layer. The broad peak suggests a larger degree of lattice imperfections or disorder, while the narrow peak signifies a more uniform and well-defined lattice structure. Additionally, the FWHM across the graded GeSn alloy was slightly higher in the middle of the gradient compared to the beginning and end. This discrepancy may arise from different growth conditions or varying degrees of strain relaxation within the alloy, leading to localized variations in crystal quality. Initially, an increase in FWHM suggests degradation in the crystal lattice due to factors like lattice

mismatch and defects. However, the subsequent reduction in FWHM at the end indicates an improvement in crystal quality, affirming the effectiveness of the Sn gradient.

Table 3. Values of strain and linewidth estimated from the Ge and GeSn diffraction peak and the values of Sn content and compressive strain estimated from the GeSn peak on the RSMs of samples ES95, ES96, and ES97.

Sample Name	Ge Buffer		GeSn Layer	
	$\varepsilon_{\parallel} \times 10^{-3}$	FWHM (deg)	Sn (%)	$\varepsilon_{\parallel} \times 10^{-3}$
ES95	−3.45	0.23	7.0	−7.10
ES96	−0.95	0.19	8.1	−5.37
ES97	0.05	0.28	10.0	−2.42
	GeSn layer − FWHM (deg)			
Position across Omega-2theta	88.25	88.83	89.5	90.0
ES97	0.67	0.73	0.67	0.28 (Broad peak) 0.06 (narrow peak)

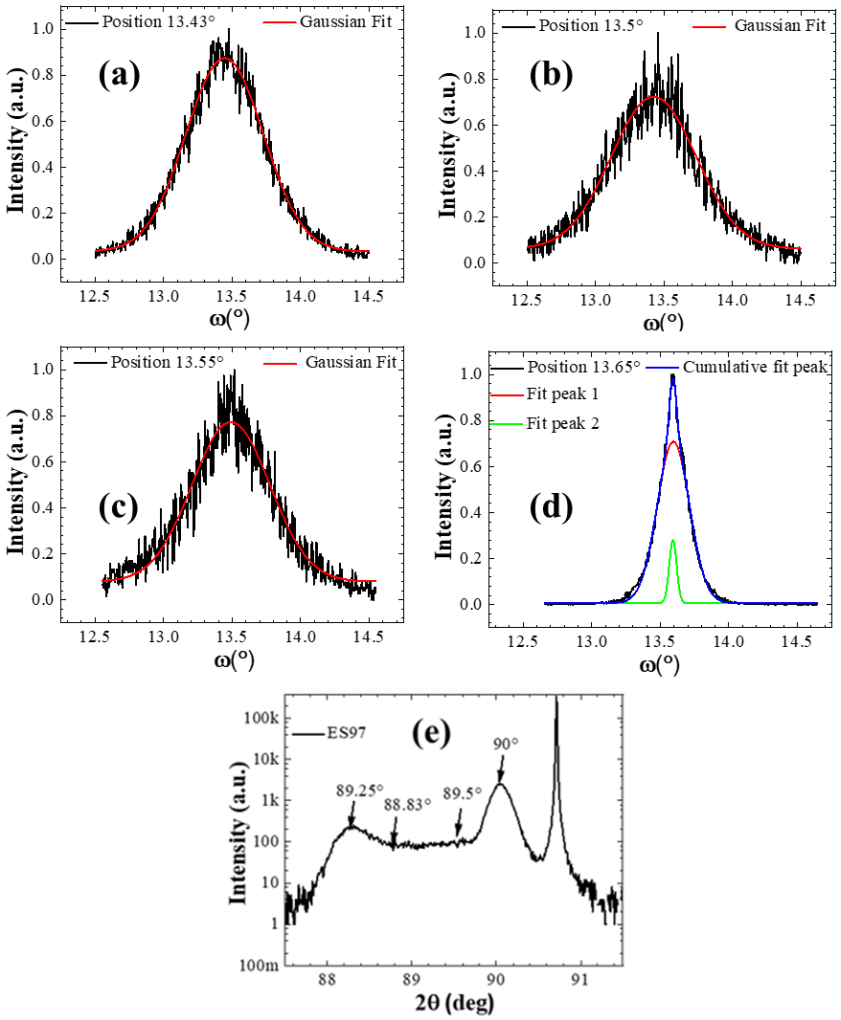

Figure 10. Gaussian-fitted Omega scan taken across the span of graded GeSn (**a**) at 89.25°, (**b**) 88.83°, (**c**) 89.5°, (**d**) Ge at 90.0° for sample ES97, and (**e**) 2Theta-Omega scan for ES97 showing the positions when Omega scans were taken.

As depicted in Figure 11, SIMS characterization was employed to validate gradient alloying for the sample ES97. The SIMS etching profile demonstrates a pronounced linear variation in $Ge_{1-x}Sn_x$ composition throughout much of the growth process, employing the algorithm applied to the Sn cell to maintain a constant Sn flux. Within a 49 min growth period, the Sn content steadily increases linearly, ranging from 0 to 8.9%. The resulting GeSn alloy achieves a thickness of 289 nm. Following the completion of the Sn gradient, within a 30 min timeframe, a minor linear gradient unfolds, elevating the Sn content from 8.9% to 9.8%, accompanied by a thickness of 120 nm under constant Sn flux. Notably, as the gradient shifts from 9.8% to 10%, the thickness further increases to 3 nm. Subsequently, the Sn gradient becomes steeper, revealing a notable increase of 4.9% with a narrow alloy thickness of 8 nm. The concurrent Ge gradient, however, exhibits a negative slope, indicating a steeper descent. This negative value in the Ge gradient suggests a propensity for Sn segregation, signifying that the germanium concentration diminishes at a more pronounced rate along the growth direction, as seen in Figure 11a. This highlights a dynamic evolution in the alloy composition and structure during this phase of the growth process. This is a consequence of strain development in the GeSn alloy. The results obtained from SIMS support the Sn concentration calculated from the RSM of sample ES97. Meanwhile, we did not observe PL from the samples, although the quality was high. This was due to the fact that we had not yet reached a Sn concentration greater than ~15%, which is required for the direct and indirect band gap to become equal under fully strained growth. Our research is now pursuing reaching a higher Sn content, either when fully strained or after relaxation.

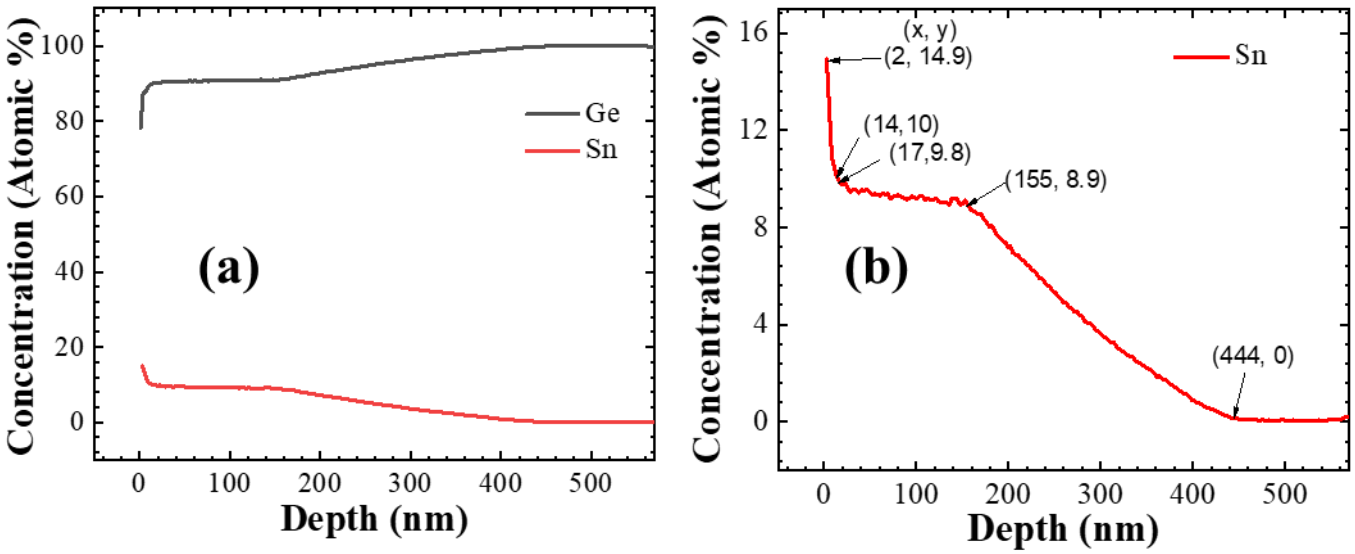

Figure 11. SIMS results for sample ES97 depict (**a**) the alloying profile of Sn and Ge concentrations versus the depth in nm and (**b**) the Sn (%) profile with an enlarged scale.

4. Conclusions

We have demonstrated that it is possible to epitaxially grow GeSn on a Ge/GaAs layer on c-plane Al_2O_3 using molecular beam epitaxy. Due to the similarity in Ge and GaAs lattice constants, the growth mode did not change, as indicated in the RHEED images. This translates into high-quality Ge with minimal FWHM. The growth of GeSn on a Ge buffer grown at 500 °C on GaAs resulted in a binary alloy with a high Sn content of 10%. The Sn incorporation was confirmed with the presence of GeSn on the Raman spectra. The algorithm used was key to controlling the grading profile of GeSn. Hence, at the end of the grading profile, the RSM showed a strong peak, indicating how GeSn continued to grow after a period of 30 min. Investigations are now underway to increase the current GeSn layer for the realization of optical measurements and, hence, device fabrication.

Author Contributions: Conceptualization, E.W., S.-Q.Y. and G.S.; methodology, E.W., C.G., S.K., H.S. and F.M.d.O.; software, E.W., F.M.d.O. and H.S.; validation, E.W., S.K. and G.S.; formal analysis, E.W., P.M.L., F.M.d.O., H.S. and Y.I.M.; investigation, E.W., C.G., M.Z.-A. and A.S.; resources, E.W., M.Z.-A. and C.G.; data curation, E.W., P.M.L., H.S., F.M.d.O. and C.G.; writing—original draft preparation, E.W., H.S. and C.G.; writing—review and editing, E.W., S.K., H.S., F.M.d.O., P.M.L., C.G., M.Z.-A., Y.I.M., S.-Q.Y. and G.S.; visualization, E.W. and H.S.; supervision, S.-Q.Y. and G.S.; project administration, S.-Q.Y. and G.S.; funding acquisition, S.-Q.Y. and G.S. All authors have read and agreed to the published version of the manuscript.

Funding: This project was funded by Navy entitled "SiGeSnPb Semiconductor Fab for Room Temp Electro- 218 Optic Infrared (IR) Sensors". Sponsor Award ID: N00014-23-1-2008. It was also funded by MURI entitled "Understanding and Breaking the Material Barriers of SiGeSn Alloys for Infrared Devices". Sponsor Award ID: FA9550-19-1-0341.

Data Availability Statement: The original contributions presented in the study are included in the article, further inquiries can be directed to the corresponding author.

Acknowledgments: We would like to acknowledge the contribution of Abdulla Said and Sudip Acharya for helping in PL measurements.

Conflicts of Interest: The authors declare no conflicts of interest.

References

1. Zhang, D.; Jin, L.; Li, J.; Wen, T.; Liu, C.; Xu, F.; Kolodzey, J.; Liao, Y. MBE growth of ultra-thin GeSn film with high Sn content and its infrared/terahertz properties. *J. Alloys Compd.* **2016**, *665*, 131–136. [CrossRef]
2. Reboud, V.; Gassenq, A.; Hartmann, J.; Widiez, J.; Virot, L.; Aubin, J.; Guilloy, K.; Tardif, S.; Fédéli, J.; Pauc, N.; et al. Germanium based photonic components toward a full silicon/germanium photonic platform. *Prog. Cryst. Growth Charact. Mater.* **2017**, *63*, 1–24. [CrossRef]
3. Jia, H.; Jurczak, P.; Yang, J.; Tang, M.; Li, K.; Deng, H.; Dang, M.; Chen, S.; Liu, H. Impact of ex-situ annealing on strain and composition of MBE grown GeSn. *J. Phys. D Appl. Phys.* **2020**, *53*, 485104. [CrossRef]
4. Kumar, R.; Saha, S.K.; Kuchuk, A.; de Oliveira, F.M.; Khiangte, K.R.; Yu, S.-Q.; Mazur, Y.I.; Salamo, G.J. Improving the Material Quality of GaAs Grown on the c-Plane Sapphire by Molecular Beam Epitaxy to Achieve Room-Temperature Photoluminescence. *Cryst. Growth Des.* **2023**, *23*, 7385–7393. [CrossRef]
5. Assali, S.; Nicolas, J.; Moutanabbir, O. Enhanced Sn incorporation in GeSn epitaxial semiconductors via strain relaxation. *J. Appl. Phys.* **2019**, *125*, 025304. [CrossRef]
6. Rathore, J.S.; Nanwani, A.; Mukherjee, S.; Das, S.; Moutanabbir, O.; Mahapatra, S. Composition uniformity and large degree of strain relaxation in MBE-grown thick GeSn epitaxial layers, containing 16% Sn. *J. Phys. D Appl. Phys.* **2021**, *54*, 185105. [CrossRef]
7. Oliveira, F.; Fischer, I.A.; Benedetti, A.; Zaumseil, P.; Cerqueira, M.F.; Vasilevskiy, M.I.; Stefanov, S.; Chiussi, S.; Schulze, J. Fabrication of GeSn-multiple quantum wells by overgrowth of Sn on Ge by using molecular beam epitaxy. *Appl. Phys. Lett.* **2015**, *107*, 262102. [CrossRef]
8. Talochkin, A.B.; Mashanov, V.I. Formation of GeSn alloy on Si(100) by low-temperature molecular beam epitaxy. *Appl. Phys. Lett.* **2014**, *105*, 263101. [CrossRef]
9. Werner, J.; Oehme, M.; Schirmer, A.; Kasper, E.; Schulze, J. Molecular beam epitaxy grown GeSn p-i-n photodetectors integrated on Si. *Thin Solid Films* **2012**, *520*, 3361–3364. [CrossRef]
10. Zhang, L.; Song, Y.; Driesch, N.v.D.; Zhang, Z.; Buca, D.; Grützmacher, D.; Wang, S. Structural Property Study for GeSn Thin Films. *Materials* **2020**, *13*, 3645. [CrossRef]
11. Zhang, Z.P.; Song, Y.X.; Zhu, Z.Y.S.; Han, Y.; Chen, Q.M.; Li, Y.Y.; Zhang, L.Y.; Wang, S.M. Structural properties of GeSn thin films grown by molecular beam epitaxy. *AIP Adv.* **2017**, *7*, 045211. [CrossRef]
12. Bhargava, N.; Coppinger, M.; Gupta, J.P.; Wielunski, L.; Kolodzey, J. Lattice constant and substitutional composition of GeSn alloys grown by molecular beam epitaxy. *Appl. Phys. Lett.* **2013**, *103*, 041908. [CrossRef]
13. Yu, K.; Zhao, Y.; Li, C.; Feng, S.; Chen, X.; Wang, Y.; Zuo, Y.; Cheng, B. The Growth of GeSn Layer on Patterned Si Substrate by MBE Method. *ECS Trans.* **2018**, *86*, 349–355. [CrossRef]
14. Wang, N.; Xue, C.; Wan, F.; Zhao, Y.; Xu, G.; Liu, Z.; Zheng, J.; Zuo, Y.; Cheng, B.; Wang, Q. Spontaneously Conversion from Film to High Crystalline Quality Stripe during Molecular Beam Epitaxy for High Sn Content GeSn. *Sci. Rep.* **2020**, *10*, 6161. [CrossRef] [PubMed]
15. Liu, T.; Wang, L.; Zhu, G.; Hu, X.; Dong, Z.; Zhong, Z.; Jia, Q.; Yang, X.; Jiang, Z. Dislocation-related photoluminescence of GeSn films grown on Ge (001) substrates by molecular beam epitaxy. *Semicond. Sci. Technol.* **2018**, *33*, 125022. [CrossRef]
16. Li, H.; Chang, C.; Chen, T.P.; Cheng, H.H.; Shi, Z.W.; Chen, H. Characteristics of Sn segregation in Ge/GeSn heterostructures. *Appl. Phys. Lett.* **2014**, *105*. [CrossRef]
17. Chen, R.; Lin, H.; Huo, Y.; Hitzman, C.; Kamins, T.I.; Harris, J.S. Increased photoluminescence of strain-reduced, high-Sn composition $Ge_{1-x}Sn_x$ alloys grown by molecular beam epitaxy. *Appl. Phys. Lett.* **2011**, *99*, 181125. [CrossRef]

18. Bonino, V.; Pauc, N.; Calvo, V.; Frauenrath, M.; Hartmann, J.-M.; Chelnokov, A.; Reboud, V.; Rosenthal, M.; Segura-Ruiz, J. Microstructuring to Improve the Thermal Stability of GeSn Layers. *ACS Appl. Mater. Interfaces* **2022**, *14*, 22270–22277. [CrossRef]
19. Wangila, E.; Lytvyn, P.; Stanchu, H.; Gunder, C.; de Oliveira, F.M.; Saha, S.; Das, S.; Eldose, N.; Li, C.; Zamani-Alavijeh, M.; et al. Growth of germanium thin film on sapphire by molecular beam epitaxy. *Crystals* **2023**, *13*, 1557. [CrossRef]
20. Gupta, N.; Mishra, A. Selection of substrate material for hybrid microwave integrated circuits (HMICs). *Energetika* **2016**, *62*, 78–86. [CrossRef]
21. Pallecchi, E.; Benz, C.; Betz, A.C.; Löhneysen, H.V.; Plaçais, B.; Danneau, R. Graphene microwave transistors on sapphire substrates. *Appl. Phys. Lett.* **2011**, *99*, 113502. [CrossRef]
22. Lu, W.; Kumar, V.; Schwindt, R.; Piner, E.; Adesida, I. DC, RF, and microwave noise performances of AlGaN/GaN HEMTs on sapphire substrates. *IEEE Trans. Microw. Theory Tech.* **2002**, *50*, 2499–2504. [CrossRef]
23. Kawagishi, K.; Komori, K.; Fukutomi, M.; Togano, K. Factors affecting the microwave surface resistance of crack-free thick YBCO films on sapphire substrates. *Phys. C Supercond. Its Appl.* **2003**, *392–396*, 1236–1240. [CrossRef]
24. Gunder, C.; Alavijeh, M.Z.; Wangila, E.; de Oliveira, F.M.; Sheibani, A.; Kryvyi, S.; Mazur, Y.I.; Yu, S.Q.; Salamo, G. Algorithm based high composition-controlled growths of GeSn on GaAs (001) via molecular beam epitaxy. *arXiv* **2023**, arXiv:2309.06695.
25. Gunder, C.; de Oliveira, F.M.; Wangila, E.; Stanchu, H.; Zamani-Alavijeh, M.; Ojo, S.; Acharya, S.; Said, A.; Li, C.; Mazur, Y.I.; et al. The growth of Ge and direct bandgap $Ge_{1-x}Sn_x$ on GaAs (001) by molecular beam epitaxy. *RSC Adv.* **2024**, *14*, 1250–1257. [CrossRef] [PubMed]
26. Moram, M.A.; Vickers, M.E. X-ray diffraction of III-nitrides. *Rep. Prog. Phys.* **2009**, *72*, 036502. [CrossRef]
27. Kim, H.J.; Duzik, A.; Choi, S.H. Lattice-alignment mechanism of SiGe on Sapphire. *Acta Mater.* **2018**, *145*, 1–7. [CrossRef]
28. Wangila, E.; Saha, S.K.; Kumar, R.; Kuchuk, A.; Gunder, C.; Amoah, S.; Khiangte, K.R.; Chen, Z.; Yu, S.-Q.; Salamo, G.J. Single crystalline Ge thin film growth on *c*-plane sapphire substrates by molecular beam epitaxy (MBE). *CrystEngComm* **2022**, *24*, 4372–4380. [CrossRef]
29. Zardo, I.; Conesa-Boj, S.; Peiro, F.; Morante, J.R.; Arbiol, J.; Uccelli, E.; Abstreiter, G.; i Morral, A.F. Raman spectroscopy of wurtzite and zinc-blende GaAs nanowires: Polarization dependence, selection rules, and strain effects. *Phys. Rev. B* **2009**, *80*, 245324. [CrossRef]
30. Grant, J.; Abernathy, G.; Olorunsola, O.; Ojo, S.; Amoah, S.; Wanglia, E.; Saha, S.K.; Sabbar, A.; Du, W.; Alher, M.; et al. Growth of Pseudomorphic GeSn at Low Pressure with Sn Composition of 16.7%. *Materials* **2021**, *14*, 7637. [CrossRef]
31. Oehme, M.; Buca, D.; Kostecki, K.; Wirths, S.; Holländer, B.; Kasper, E.; Schulze, J. Epitaxial growth of highly compressively strained GeSn alloys up to 12.5% Sn. *J. Cryst. Growth* **2013**, *384*, 71–76. [CrossRef]
32. Slav, A.; Dascalescu, I.; Lepadatu, A.-M.; Palade, C.; Zoita, N.C.; Stroescu, H.; Iftimie, S.; Lazanu, S.; Gartner, M.; Buca, D.; et al. GeSn/SiO_2 Multilayers by Magnetron Sputtering Deposition for Short-Wave Infrared Photonics. *ACS Appl. Mater. Interfaces* **2020**, *12*, 56161–56171. [CrossRef] [PubMed]
33. Liu, T.; Miao, Y.; Wang, L.; Zhu, G.; Hu, H.; Zhong, Z.; Yang, X.; Jiang, Z. Temperature dependence of Raman scattering in GeSn films. *J. Raman Spectrosc.* **2020**, *51*, 1092–1099. [CrossRef]
34. Oehme, M.; Kostecki, K.; Schmid, M.; Oliveira, F.; Kasper, E.; Schulze, J. Epitaxial growth of strained and unstrained GeSn alloys up to 25% Sn. *Thin Solid Films* **2014**, *557*, 169–172. [CrossRef]
35. Nakamura, M.; Inagaki, S.; Okamura, Y.; Ogino, M.; Takahashi, Y.; Adachi, K.; Hashizume, D.; Tokura, Y.; Kawasaki, M. Band structures in orientation-controlled CuI thin films under epitaxial strain. *Phys. Rev. B* **2022**, *106*, 125307. [CrossRef]

Disclaimer/Publisher's Note: The statements, opinions and data contained in all publications are solely those of the individual author(s) and contributor(s) and not of MDPI and/or the editor(s). MDPI and/or the editor(s) disclaim responsibility for any injury to people or property resulting from any ideas, methods, instructions or products referred to in the content.